

Danmarks Tekniske Universitet

DEPARTMENT OF NATIONAL SPACE INSTITUTE

---

PROJECT: PYRAMIDAL HORN  
ANTENNA

*Advanced Antenna Techniques and Measurements*

Authors:

Tomás Ruiz Aybar, s242887

Niyaz Mahmud Sayem, s240041

December 8, 2024

# Index of Contents

<b>1</b>	<b>Introduction</b>	<b>3</b>
<b>2</b>	<b>Analysis of results</b>	<b>3</b>
2.1	Theoretical Analysis . . . . .	4
2.1.1	ka-band pyramidal horn [26.5 - 40] GHz . . . . .	6
2.1.2	C-band pyramidal horn [3.95 - 5.85]GHz . . . . .	8
2.2	Simulated Analysis . . . . .	8
2.2.1	ka-band pyramidal horn [26.5 - 40] GHz . . . . .	9
2.2.2	C-band pyramidal horn [3.95 – 5.85] GHz . . . . .	11
2.3	Experimental Analysis . . . . .	12
2.3.1	Ka-band, NSI-MI/Ametek mm-wave chamber . . . . .	13
2.3.2	Experimental Analysis, C-Band . . . . .	15
2.4	Final comparison . . . . .	16
2.4.1	ka-band comparison . . . . .	16
2.4.2	C-band comparison . . . . .	17
<b>3</b>	<b>Conclusion</b>	<b>18</b>
<b>A</b>	<b>Appendix</b>	<b>19</b>

## List of Figures

1	Pyramidal Horn design. Source[X] . . . . .	3
2	Theoretical pattern obtained for the Ka-band SGH through the equations in [2] . . . . .	6
3	Ka-band AUT pattern analysis. . . . .	7
4	HPBW and FSLL parameters of the Ka-band pyramidal horn. . . . .	7
5	C-band AUT pattern analysis, E and H-planes copolar components. . . . .	8
6	Antenna Design in HFSS with isometric view. . . . .	9
7	Antenna Simulated Paramter . . . . .	9
8	Co and Cross-polar components for E and H-Planes, Ka-band. . . . .	10
9	C-band AUT simulated parameters results . . . . .	11
10	Co and Cross-polar components for E and H-Planes, C-band . . . . .	12
11	Set of facilities and components required for the ka-band experimental test. . . . .	13
12	ka-band AUT experimental pattern analysis. . . . .	14
13	HPBW and FSLL parameters of the experimental Ka-band pyramidal horn. . . . .	14
14	Set of facilities and components required for C-band Experiment. . . . .	15
15	Experimented Analysis of C-band Horn Antenna . . . . .	16
16	Ka-band radiation pattern comparison between the theoretical, simulated and experimental results. . . . .	17
17	C-band radiation pattern comparison between the theoretical, simulated and experimental results. . . . .	18
18	Different Ka-band parameters obtained through HFSS. . . . .	22
19	Different C-band parameters obtained through HFSS. . . . .	22

## List of Tables

1	Dimensions of the two AUT. . . . .	4
2	Balanis [2] equations needed to compute theoretical results. . . . .	5
3	Comparison of radiation pattern parameters for different calculation methods. . . . .	8
4	Comparison of radiation pattern parameter, theoretical vs simulated. . . . .	12
5	Comparison of radiation pattern parameters, theoretical vs simulated vs experimental. . . . .	16

## 1 Introduction

This project explores the analysis of pyramidal horn antennas within the Ka (26. 5-40 GHz) and C (3. 95-5. 85 GHz) frequency bands through a comprehensive blend of theoretical, simulated, and experimental methodologies. The theoretical phase focuses on developing ideal models that predict crucial parameters. During the simulation phase, sophisticated tools like HFSS are utilized to investigate further dimensions, such as diffraction effects and the impact of meshing on performance. Lastly, experimental measurements conducted in anechoic chambers provide a practical perspective, revealing how the antennas operate in real-world conditions and serving to validate the theoretical and simulated models.

## 2 Analysis of results

This section will present a complete analysis of the results obtained by three different approaches for studying two Standard Gain Horns (SGHs) associated with two other frequency bands. The Antenna Under Test (AUT) follows a pyramidal horn's well-known configuration, as stated in Figure 1. Furthermore, the dimensions of each AUT will define and characterize the frequency range where they operate; the two bands to be studied are *Ka-band* and *C-band*, which correspond to the frequency ranges of [26.5 - 40]GHz and [3.95 - 5.85]GHz, respectively. Table 1 shows each of the dimensions for the two antennas, showing how the one with larger extensions corresponds to smaller frequencies; therefore, the one with smaller dimensions is linked to the higher frequency range.

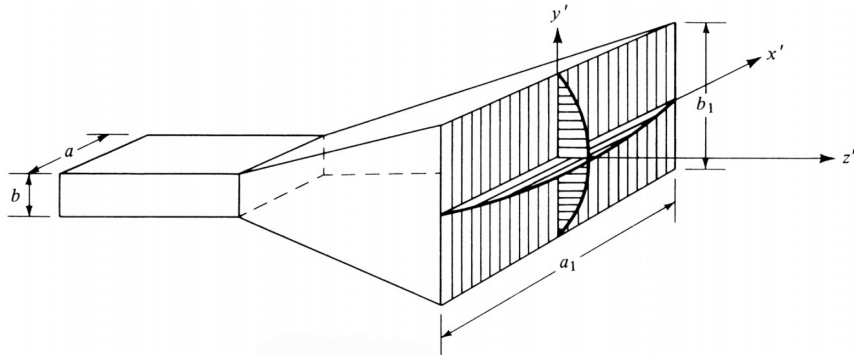


Figure 1: Pyramidal Horn design. Source[X]

Band	C-band [GHz]	Ka-band [GHz]
Frequency range	3.95 - 5.85	26.5 - 40
Dimensions [mm]		
Waveguide width, $a$	47.55	7.112
Waveguide height, $b$	22.20	3.556
Waveguide length, $l$	68.00	31.50
Wall thickness, $w$	8.40	1.00
Aperture width, $a_1$	216.00	68.50
Aperture height, $b_1$	160.00	56.50
Horn length, $L$	240.00	150.00

Table 1: Dimensions of the two AUT.

Subsequently, these two SGHs will be analysed by a theoretical approach, by simulations computed with a commercial 3D electromagnetism simulator as HFSS, and by experimental measurements obtained in anechoic chambers MVG SG EVO and NSI-MI/Ametek mm-wave.

## 2.1 Theoretical Analysis

During this theoretical analysis, important and typical antenna parameters will be studied for the AUTs—parameters such as the pattern, directivity, beamwidth, side lobe level (SLL) and cross-polarization. Without going into too much detail on the theory of SGH, some expressions of high relevance are going to be commented to understand the process that has been followed to obtain theoretical results for both pyramidal horn antennas based on their dimensions alone.

First of all, it is very important to highlight that all the formulas that are going to be listed below are based on the *Huygens equivalence principle*, since horns are theoretically treated as aperture antennas. Hence, there will be some equivalent currents on the aperture that can be approximated by the waveguide fundamental mode ( $TE_{10}$ ), and the fields outside it are set to zero.

The expressions that have been implemented for this theoretical approach, which will allow us to have some first solid results to compare with future simulated and experimental data, are those that compute the far zone E-field radiated by a pyramidal horn in spherical coordinates. Equations 1, 2, 3 correspond to (13-46a) to (13-46c) from [2].

$$E_r = 0, \quad (1)$$

$$E_\theta = -j \frac{kE_0 e^{jkr}}{4\pi r} [\sin\phi(1 + \cos\theta) I_1 I_2], \quad (2)$$

$$E_\phi = j \frac{kE_0 e^{jkr}}{4\pi r} [\cos\phi(\cos\theta + 1) I_1 I_2]. \quad (3)$$

Using the previous formulas, alongside the directivity (4), will allow us to account for most of the parameters of interest. This expression for the directivity is also found in [2] as (13.50),

$$D_p = \frac{8\pi\rho_1\rho_2}{a_1 b_1} \left\{ [C(u) - C(v)]^2 + [S(u) - S(v)]^2 \right\} \times \left\{ C^2 \left( \frac{b_1}{\sqrt{2\lambda\rho_1}} \right) + S^2 \left( \frac{b_1}{\sqrt{2\lambda\rho_1}} \right) \right\}. \quad (4)$$

Nevertheless, to achieve some results from these expressions directly with the information stated in Table 1, a large number of intermediate calculations must be carried out to complete

the calculation process. Among them, the following stand out:  $I_1$ ,  $I_2$ ,  $\rho_1$ ,  $\rho_2$ ,  $C(u)$ ,  $C(v)$ ,  $S(u)$  and  $S(v)$ ; Table 2 displays where these formulas can be founded in [2].

Parameter	Balanis Equation
$I_1$	(13.44)
$I_2$	(13.45)
$C(u)$	Cosine Fresnel integral of (13.39a)
$C(v)$	Cosine Fresnel integral of (13.39b)
$S(u)$	Sine Fresnel integral of (13.39a)
$S(v)$	Sine Fresnel integral of (13.39b)

Table 2: Balanis [2] equations needed to compute theoretical results.

Likewise, to calculate specific values for  $\rho_1$  and  $\rho_2$  explicit equations that relate SGH's dimensions/parameters between each other are needed. Expressions 5 and 6 have been obtained by applying similarity of triangles over 1,

$$\rho_1 = \sqrt{\rho_e^2 - \frac{b_1^2}{4}}, \quad (5)$$

$$\rho_2 = \sqrt{\rho_h^2 - \frac{a_1^2}{4}}. \quad (6)$$

Where  $\rho_e$  and  $\rho_h$  can be obtained by (13-47a) and (13-47b) from [2] as

$$\rho_e = b_1 \left[ \left( \frac{p_e}{b_1 - b} \right)^2 + \frac{1}{4} \right]^{\frac{1}{2}} \text{ and} \quad (7)$$

$$\rho_h = a_1 \left[ \left( \frac{p_h}{a_1 - a} \right)^2 + \frac{1}{4} \right]^{\frac{1}{2}}. \quad (8)$$

It can be easily seen that both values can be computed directly with information which is already known from Table 1, the AUTs dimensions ( $p_e, p_h, a_1, a, b_1$ , and  $b$ ). Another two assumptions that have been made are related to the  $E_0$  magnitude and the distance  $r$ ;  $E_0$  has been chosen equal to 1 for simplicity. However, this is unimportant as the represented fields will be normalized to their maximum value and concerning the resultant directivity. On the other hand, the distance  $r$  has been selected so it verifies the Far Field (FF) conditions; according to *Rayleigh distance*, which is  $\frac{2D}{\lambda}$ ,  $r$  has been selected as double of this distance.

Finally, once all the mathematical procedures have been completed, it will be able to graphically represent the results. To plot the E-field resultant pattern for the copolar and cross-polar components we have used the *Ludwig's 3'rd* definition for linear polarization, so  $E_\theta$  and  $E_\phi$  are now used to compute  $E_{co,3L}$  and  $E_{cx,3L}$  as

$$E_{co,3L} = E_\theta \cos(\phi - \phi_0) - E_\phi \sin(\phi - \phi_0), \quad (9)$$

$$E_{cx,3L} = E_\theta \sin(\phi - \phi_0) + E_\phi \cos(\phi - \phi_0). \quad (10)$$

Appendix A contains all the Code 1 that has been designed to carry out this theoretical process capable of calculating the radiated fields of a pyramidal horn antenna through the method

of equivalent currents (*Huygens equivalence principle*). For instance, the pattern obtained for the Ka-band AUT is shown in Figure 2 from below.

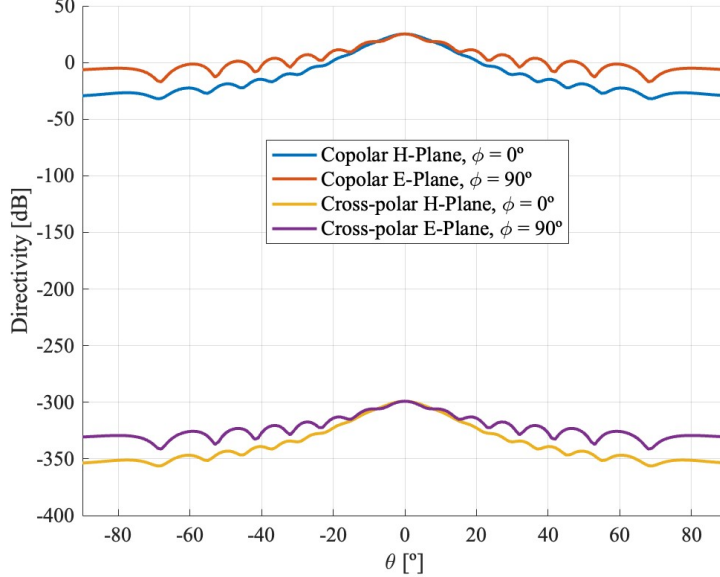


Figure 2: Theoretical pattern obtained for the Ka-band SGH through the equations in [2]

The detailed analysis of each parameter of interest for the two AUTs will begin.

### 2.1.1 ka-band pyramidal horn [26.5 - 40] GHz

This linearly Y-polarized horn has several noteworthy behaviours, they can be analyzed from different parameters through several plots of the radiation pattern ("Spatial distribution of a quantity that characterizes the electromagnetic field generated by an antenna", [3]) that show each of them. For instance, Figure 2, states the two *Ludwig's 3'rd* components ( $E_{co,3L}, E_{cx,3L}$ ) of the main planes, E and H-plane of the AUT. It can be seen how the cross-polar components have an amplitude level that reaches -300 dB, which in linear amplitudes is practically equal to zero. This event is caused by the theoretical assumption that the horn is completely symmetrical, so that, as it is said in [2], if it is excited in the dominant mode, there should be no field component radiated by the antenna which is orthogonal to the main polarization (cross-pol),  $E$  is directly proportional to  $E_{co}$ .

Nevertheless, we can precisely measure the directivity obtained in the copolar components. Directivity is defined by [3] as *the ratio of the radiation intensity in a given direction from the antenna to the radiation intensity averaged over all directions*; in Figure 3a it has been attached a zoomed radiation pattern where the two principal planes behaviour can be perfectly seen. The maximum level of directivity is 24.4892 dB (this value has been obtained for the intermediate frequency fo the ka-band range). In addition, it should be noted how the pattern is very narrow in both principal planes; this horn contains a sinusoidal amplitude distribution in the x direction and quadratic phase variations in the x and y directions, this cosine taper by the  $TE_{10}$ -mode results in a wider and more constant E-plane pattern as  $\theta$  increases, due to the maximum of the original field distribution in the aperture ( $E_y$ ) coincides with the E-plane alignment ( $\phi = 90$ ).

Similarly, the H-plane pattern decreases faster with  $\theta$ ; this reasoning can be corroborated through Figure 3b

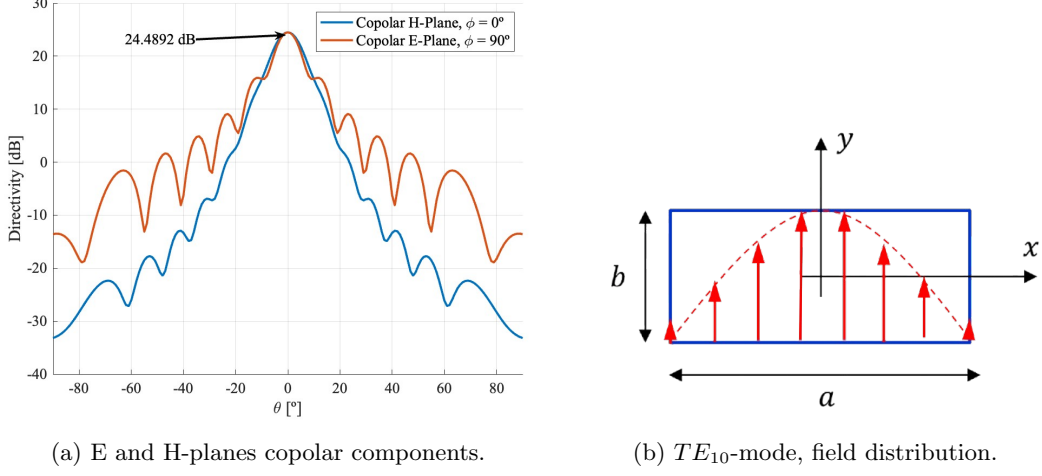


Figure 3: Ka-band AUT pattern analysis.

If we continue with the detailed analysis of this radiation pattern between  $-90 \leq \theta \leq 90$ , for this particular AUT, parameters such as beamwidth or first side lobe level (FSLL) can be studied. The first of these will be studied utilizing the *Half-Power-Beam-Width* (HPBW), which is defined as "*In a plane containing the direction of the maximum of a beam, the angle between the two directions in which the radiation intensity is one-half value of the beam.*" To measure this parameter it is sufficient to visualise for which theta a radiation level equal to the maximum -3dB is obtained, because  $-3dB = 10\log_{10}(0.5)$ . Figure 4 shows that the resultant HPBW is equal to  $9^\circ$ . Regarding the FSLL, which will indicate the level of the first secondary lobe (SLL) concerning the maximum level of the main lobe; its value has been found at 15.6825 dB, which implies a FSLL equal to -8.807 dB.

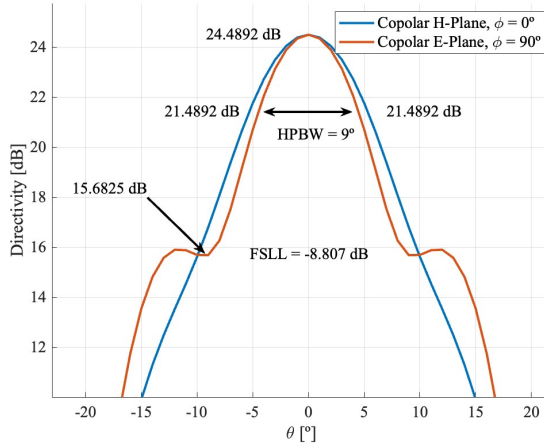


Figure 4: HPBW and FSLL parameters of the Ka-band pyramidal horn.

### 2.1.2 C-band pyramidal horn [3.95 - 5.85]GHz

For this second AUT working in the C-band, a completely analogous analysis process has been performed for all parameters that can be obtained from the radiation pattern of this horn. In this case, the intermediate frequency has been used again, 4.9GHz, and the final results obtained are shown in figure 5 and table 3, through which identical conclusions have been drawn for each parameter. This table will be completed throughout the report with the results obtained in the simulation and experimental phases as a comparison between all of them.

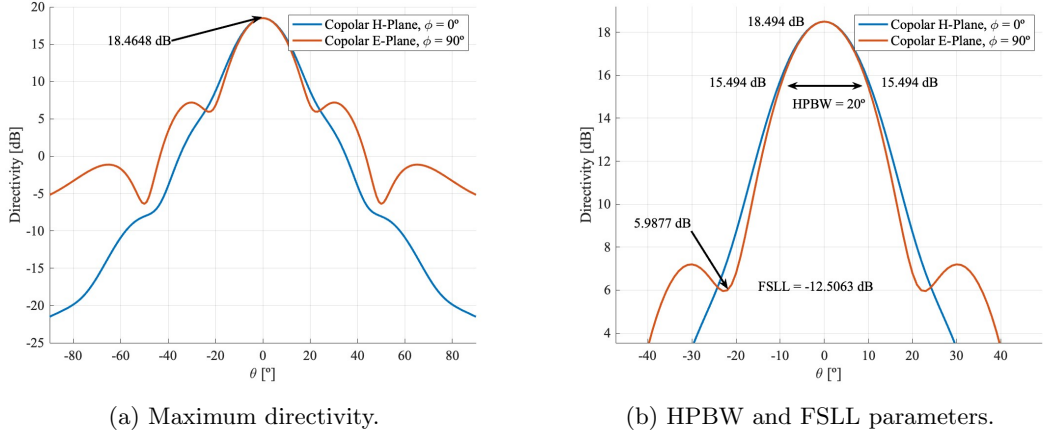


Figure 5: C-band AUT pattern analysis, E and H-planes copolar components.

AUT	Ka-band [26.5 - 40]GHz			C-band [3.95 - 5.85]GHz		
Parameter	$D_{max}$ [dB]	HPBW [°]	FSLL [dB]	$D_{max}$ [dB]	HPBW [°]	FSLL [dB]
Theoretical	24.489	9	-8.807	18.465	20	-12.506

Table 3: Comparison of radiation pattern parameters for different calculation methods.

## 2.2 Simulated Analysis

HFSS essentially employs the Method of Moments (MoM) technique for RF field computations. With HFSS, the overall antenna structure can be segmented into small tetrahedral-shaped meshes. In each of the elements, mathematical functions approximate the electromagnetic fields. Local field distributions are obtained for each element using Maxwell's equations. These local solutions are then compiled in a global matrix equation which prescribes the overall structure. Furthermore, HFSS utilises MoM along with Integral Equation (IE) solvers in open regions. MoM computes fields on conductors or dielectric interfaces and surface currents on the conductors or dielectric interfaces to determine the fields in space. We are not getting deeper with the equation here. At this point we started designing the Hron Antenna for the C band at 3.95 – 5.85 GHz and the Ka band at 26.5 – 40 GHz.

Following the process of designing the Horn Antenna, we designed and simulated it, which can be seen from Figure 6a below.

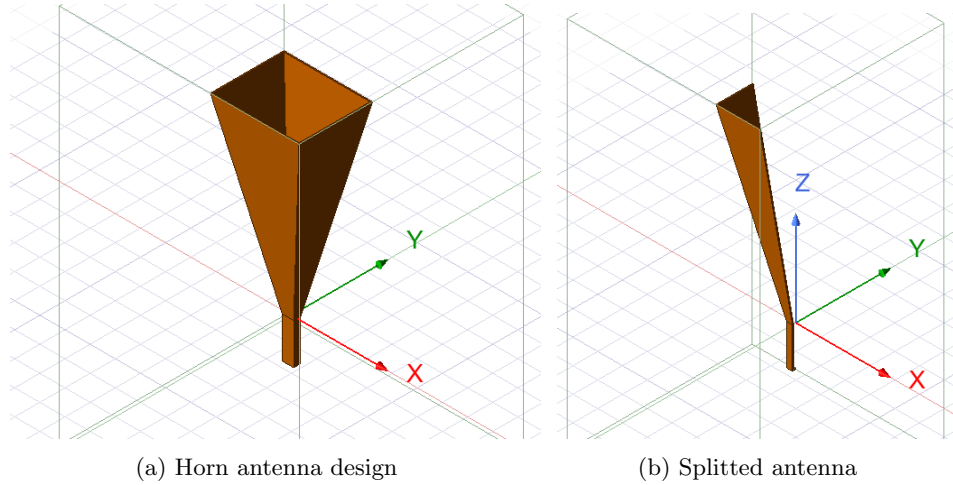


Figure 6: Antenna Design in HFSS with isometric view.

Following the instructions after completing the design, we were able to process the simulation's results.

### 2.2.1 ka-band pyramidal horn [26.5 - 40] GHz

E-plane and H-plane radiation patterns are important features in understanding the characteristics of pyramidal horn antennas. A more detailed account of the diffraction influences such as at the aperture edges is important for correct estimation of the field intensity in the minor lobes of radiation patterns and for also reducing cross-polarization. From Figure 7, we analyze the radiation pattern of a pyramidal horn antenna, with directivity (dB) plotted against the angular position  $\theta$  in degrees where the blue is the copolar H plane  $\phi = 0$  and the orange one is the copolar E plane  $\phi = 90^\circ$ . The co-pol directivity reaches its maximum around  $0^\circ$  indicating the direction of the main beam and we achieved 24.6529 dB at 0 degree for both. This peak suggests that it is highly directional. Whereas the cross-polar components are lower than expected (Figure 8).

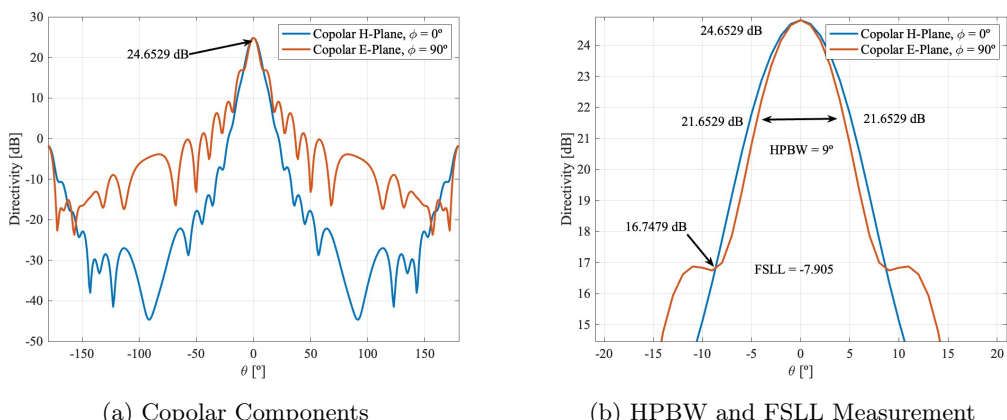


Figure 7: Antenna Simulated Parameter

It is seen from the co-polar curve that there are several small lobes on either side of the main lobe curve with lower directivity at higher values of  $\theta$ . These sidelobes appear to arise from edge diffraction and are characteristic of horn antennas. Again, the cross-pol component is noticed to be lower than the co-pol over a broad range of angles. In this case, this suggests good polarization purity as the cross-polarization is reduced to the barest minimum. We also observe that both co-pol and cross-pol patterns replicate each other concerning  $\theta=0$  degree due to the geometric orientation of the antenna at higher  $\theta$ . These sidelobes indicate edge diffraction effects and are expected for horn antennas. The cross-pol component remains significantly lower than the co-polar across most of the angular range. This indicates good polarization purity, as the cross-polarization levels are minimized. Both co-pol and cross-pol patterns are symmetric around  $\theta=0$  degree, reflecting the symmetry of the antenna's geometry. In summary, this radiation pattern proves that horn antenna has high directivity, unexpected low cross polarisation which can be seen from Fig. 8 and the side lobe structure as predicted by aperture edge diffraction.

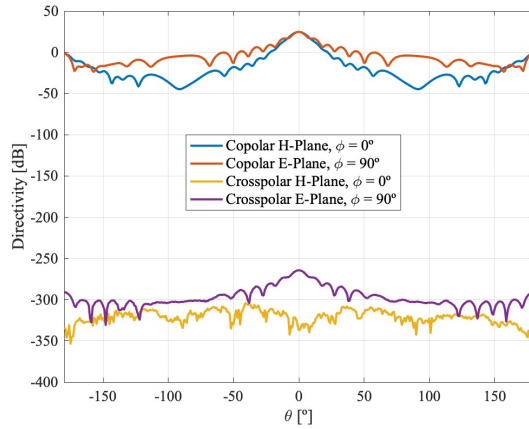


Figure 8: Co and Cross-polar components for E and H-Planes, Ka-band.

We discussed with Professor Javier the fact of low cross-polarization and got some information that to solve the whole Horn structure, HFSS divides space into a stepped format, which is called tetrahedral, wherein every one of them solves field equations and all are summed to get the total field of the antenna. However, because the meshing is somewhat arbitrary, and not aligned along any direction the whole element also adds a bit of cross-polar component to the combination which is what is evidenced in the patterns that are included at the end of the prescription instruction manual. In the same case when we are adding the symmetry planes a certain portion of the structure is only added in the quarter and then the solution is obtained by reflecting the solved portion on the planes. This also makes the solution symmetric, therefore the cross-polar component from the mesh elements almost cancels with the mirror contribution, and this gives a pattern cross-polar in the order of numerical noise all over the pattern.

HFSS also provides for diffracted rays and fringing effects that prevail in most regions around the horn aperture zone. This enabled cross-polarization components to occur naturally because the aperture of the horn is not modelled as an ideal infinite ground plane. Applying the same to Ludwig's 3rd definition we can define co-polarized and cross-polarized components. Other types of representations (3D radiation pattern, Figure 18a) and parameters such as  $S_{11}$  have been easily analyzed through HFSS. For instance, the  $S_{11}$  plot (Figure 18b) provided in the Appendix shows the reflection coefficient of the horn antenna over the frequency range of 26.5 GHz to 40

GHz. The S11 values remain consistently below -28 dB across the band, indicating excellent impedance matching and minimal power reflection.

### 2.2.2 C-band pyramidal horn [3.95 – 5.85] GHz

We designed a C-band with the mentioned dimension (Table 1) for this project where the antenna operates at a centre frequency of 4.9 GHz. The orthogonal nature of the currents in the E-plane ( $\phi = 90^\circ$ ) provides a maximum directivity of 18.8049 dB with a narrow main beam and suppressed side lobe levels shown in Fig. 9a. The H-plane ( $\phi = 0^\circ$ ) also exhibits a full bar and reliable radiation pattern as the E-plane. Such patterns reflect some sort of symmetry, which also points to the antenna's overall balanced construction. The suppression of side lobes also helps to generally improve the constellation performance, with the co-polarization superior to cross-polarization over a broad angular range. In combination with high directivity, low cross-polarization, and well-controlled side lobes; this antenna works very well for C-band applications. We already mentioned briefly in Ka-band about the unexpected cross-polarization.

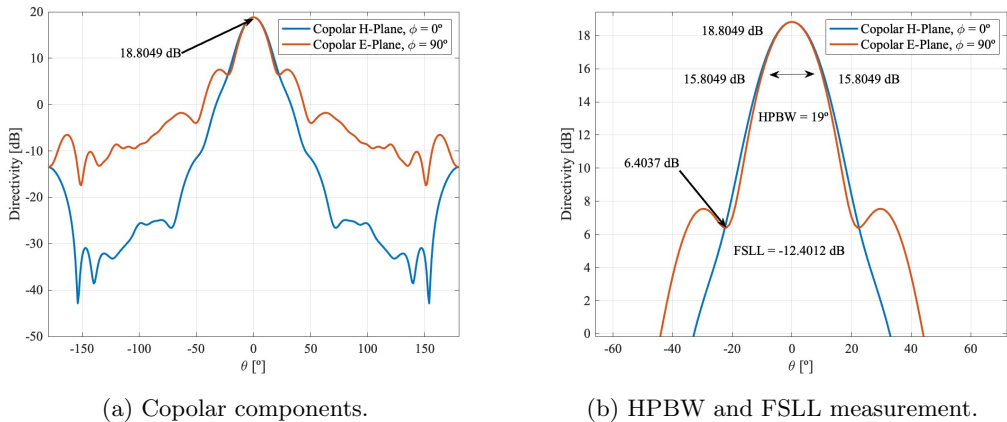


Figure 9: C-band AUT simulated parameters results

These simulation results at the C-band pyramidal horn antenna reveal a Half Power Beamwidth (HPBW) of 19 degrees, thus demonstrating the capability of the model to generate a tight beam, wider than the Ka-band one. The values of the First Side Lobe Level (FSLL) characterized the effectiveness of side lobe suppression and reduction of interference from undesired directions: FSLL = -12.4dB.

It appears vividly that the simulation shows very low cross-polarization in Fig. 10 levels for both E-plane and H-plane. This low cross-polarization is highly desirable because it means that the antenna can provide good polarization purity which is the key characteristic of the antenna.

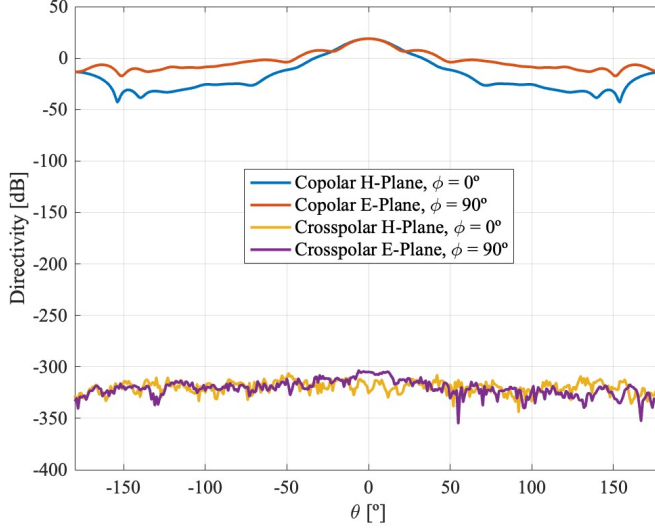


Figure 10: Co and Cross-polar components for E and H-Planes, C-band

Once again, the  $S_{11}$  graph and a 3D radiation pattern for this C-band pyramidal horn has been attached in the Appendix (Figure 19).

AUT	Ka-band [26.5 - 40]GHz			C-band [3.95 - 5.85]GHz		
Parameter	$D_{max}$ [dB]	HPBW [°]	FSLL [dB]	$D_{max}$ [dB]	HPBW [°]	FSLL [dB]
Theoretical	24.489	9	-8.807	18.465	20	-12.506
Simulated	24.653	9	-7.905	18.805	19	-12.401

Table 4: Comparison of radiation pattern parameter, theoretical vs simulated.

### 2.3 Experimental Analysis

Finally, there is one more way to test and study these two SHGs: experimentally measuring both AUTs in RF anechoic chambers. These rooms try to emulate free-space conditions by using pyramidal RF absorbers. In this case, for the two different antenna test ranges, we have obtained real horn antenna measurements using DTU-ETC facilities, MVG SG EVO and NSI-MI/Ametek mm-wave, for the C-band and Ka-band, respectively.

Both setups make use of highly advanced near-field measurement techniques and DSP methods. To be more specific, we are dealing with Spherical near-field measurements, this technique is based on three different main steps that will allow us to analyze the far-field pattern from these near-field measurements. Those three steps are [1]:

1. Data acquisition of the tangential components of the near field around the AUT on a spherical surface with a radius  $R < a$ . Fulfilling the following sampling criteria

$$\Delta\theta = \Delta\phi = \frac{360}{2N + 1}.$$

2. Solve the Spherical Wave Expansion (SWE) by the Fourier method to calculate the Q-coefficients.

3. Once this information is gathered, we can compute the far-field ( $r \rightarrow \infty$ )  $E$  pattern of the AUT, from which different pattern parameters can be studied.

The following describes each of the environments in which each of the AUTs was measured, together with an analysis of the results obtained in these environments.

### 2.3.1 Ka-band, NSI-MI/Ametek mm-wave chamber

For the Ka-band range [26.5-40]GHz we have measured a pyramidal horn antenna in the NSI-MI/Ametek mm-wave anechoic chamber. The set-up of this chamber (Figure 11) is based on two separated main arms that are perfectly aligned to get an ideal spherical measurement system with a coinciding point that must correspond to the centre of the "sphere". One arm holds the AUT while the second one contains the probe; the AUT arm is fixed, whereas the probe arm can turn along the  $\theta$  and  $\phi$  axis,  $[-75 \leq \theta \leq 75]$  and  $[0 \leq \phi \leq 180]$  respectively. The probe has an imaginary axis perpendicular to the AUT's aperture, always pointing to the centre point of the horn. Thus, the probe's aperture will always be tangential to the sphere surface, corresponding to the tangential components that need to be measured.

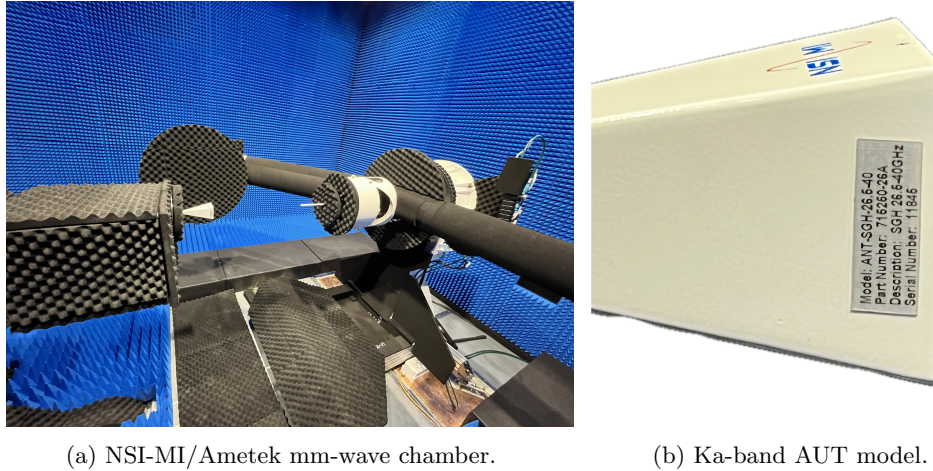


Figure 11: Set of facilities and components required for the ka-band experimental test.

Figure 11b shows the label of the AUT pyramidal horn measured, in this case, it was the model "*ANT-SGH-26.5-40*" with a serial number equal to 11846. This antenna was measured at three different frequencies, corresponding to the range's minimum, intermediate, and maximum frequency. In this analysis, we will mainly focus on the intermediate frequency at 32.5 GHz, nevertheless, we have illustrated a pattern comparison of the principal E-plane at Figure 12a where it can be seen how the resultant pattern will have a narrower beamwidth every time frequency is increased, however, in the same way the FSLL will be higher (less amplitude distance between the maximum and this point). In addition, Figure 12b states the resultant pattern for this experimental measurement of the Ka-band pyramidal horn antenna; the maximum directivity is obtained at 24.473dB and the cross-polar components are found to be -4.14dB, which can be

translated into a difference of -28dB, it indicates that the cross-polar component is significantly weaker than the copolar component. It is salient to note that these experimental results are limited by the physical limitations of the setup, which was only capable of measuring from  $-75^{\circ}$  to  $75^{\circ}$  in the theta axis, hence we just can trust the results until the  $\theta_{min}$  and  $\theta_{max}$  shown in Figure 12b.

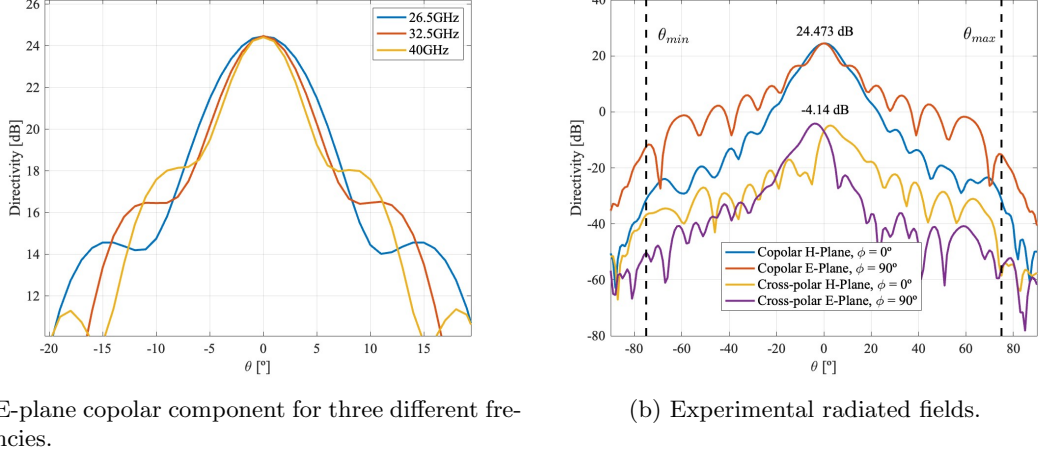


Figure 12: ka-band AUT experimental pattern analysis.

Again, the remainder of the analysis will focus on the parameters of interest from the radiation pattern attached below (Figure 12b). After studying a zoomed version of it, the resulting HPBW is equal to  $9^{\circ}$  again, and the FSLL has been found at -8.006dB; both parameters can be seen at Figure 13.

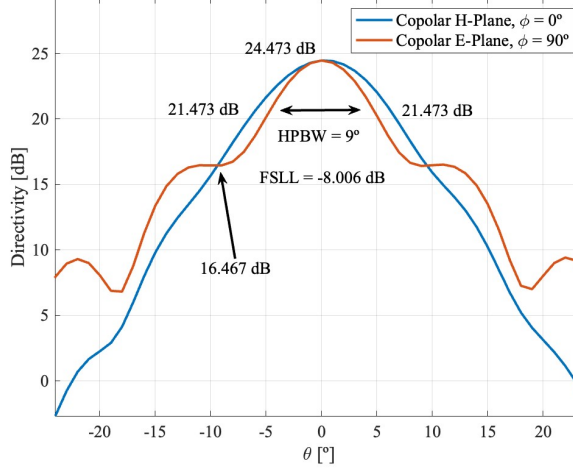
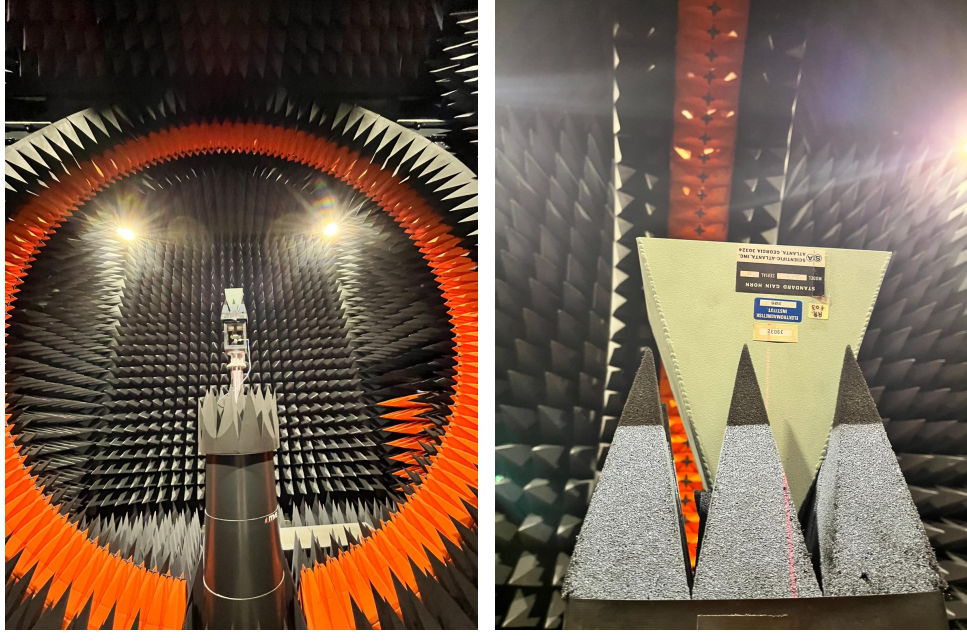


Figure 13: HPBW and FSLL parameters of the experimental Ka-band pyramidal horn.

### 2.3.2 Experimental Analysis, C-Band

A central pedestal mounts the Antenna Under Test, which can rotate and be raised or lowered vertically.  $\phi$  is the rotation angle of the pedestal and  $\theta$  is around the static orange circle that surrounds the AUT shown in Figure 14a. Though the orange circle itself is stationary, the probes mounted on it can shift slightly clockwise when taken from the system's door. This small movement in the probes allows for more precise angular movements of the probes so that measurements can be made finer-grained than would otherwise be possible with stationary probes. The orange circle is each probe, and the two antennas inside each probe are represented with a small 'plus sign' structure. They use dual antennas to measure the polarization states of the signals. The system consists of 69 ports, of which 68 are for measurement probes and 1 is a reference port. But the orange circle lacks a bottom where the pedestal is placed. There is a gap at the bottom where the pedestal is placed so we cannot place a probe, and therefore cannot measure at the bottom. The model number for our experimented C-Band Antenna is 12-3.9 shown in Figure 14b.



(a) C-Band Measurement Setup.

(b) C-band AUT model.

Figure 14: Set of facilities and components required for C-band Experiment.

To demonstrate various pattern, a C-band horn antenna is depicted with co-polarization (Co-Pol) and cross-polarization (Cross-Pol) patterns of its directivity as a function of the angle  $\theta$  measured in dB. At this frequency, the CoPol pattern has the main lobe at  $\theta = 0$  degree, whose peak directivity is approximately 18.7 dB with a symmetric fall off at wider angles and shows radiation characteristics of the beam in Figure 15a. In contrast, the Cross-pol pattern, the undesired orthogonal polarization, has very low directivity levels with good polarization purity, there is a -30.33dB between both components. Even at wider angles, the sidelobes in the Cross-Pol pattern are much lower than the Co-Pol and, as a result, provide a high Co-Pol to Cross-Pol ratio. Once this polarization performance is shown, this efficiency and suitability for

C band applications becomes evident. With a zoom section we can see the HPBW and FSLL from Figure 15b.

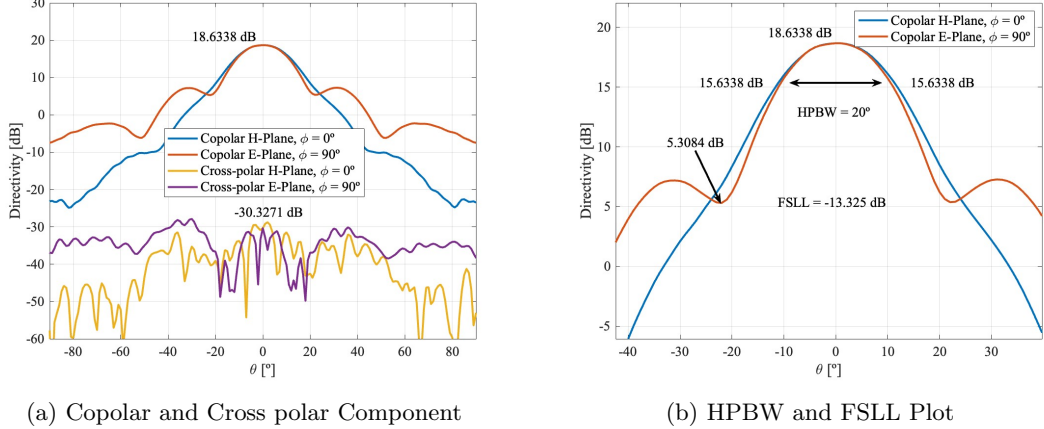


Figure 15: Experimented Analysis of C-band Horn Antenna

These key performance parameters are demonstrated in the experimental results from the C-band horn antenna with a Half Power Frequency Beamwidth (HPBW) of 20 degrees and a First Sidelobe Level (FSLL) of -13.325 dB.

## 2.4 Final comparison

Finally, after having analysed both AUTs under different circumstances, theoretically, simulated by commercial 3D-EM software and experimentally in free-space conditions, we can directly compare each of the resultant patterns to figure out a proper conclusion about the existence difference between the three different scenarios stated along this project. Once again, the comparison will be done separately according to the two frequency bands studied.

AUT	Ka-band [26.5 - 40]GHz			C-band [3.95 - 5.85]GHz		
Parameter	$D_{max}$ [dB]	HPBW [°]	FSLL [dB]	$D_{max}$ [dB]	HPBW [°]	FSLL [dB]
Theoretical	24.489	9	-8.807	18.465	20	-12.506
Simulated	24.653	9	-7.905	18.805	19	-12.401
Experimental	24.473	9	-8.006	18.634	20	-13.325

Table 5: Comparison of radiation pattern parameters, theoretical vs simulated vs experimental.

### 2.4.1 ka-band comparison

To compare the behaviour of the AUT radiation pattern in the different scenarios, we will split them into two main planes (E and H-plane), so we can clearly distinguish the differences obtained at each. Figure 16 shows the comparison for these two planes, it can be seen how the three copolar components are very close to each other and their maximum directivity level is almost the same, as stated in Table 5, this small difference corresponds with a relative error equal to 0.73%. Furthermore, it must be noted that this comparison can only be fairly made until  $-75 \leq \theta \leq 75$ , due to the physical constraints of the experimental setup.

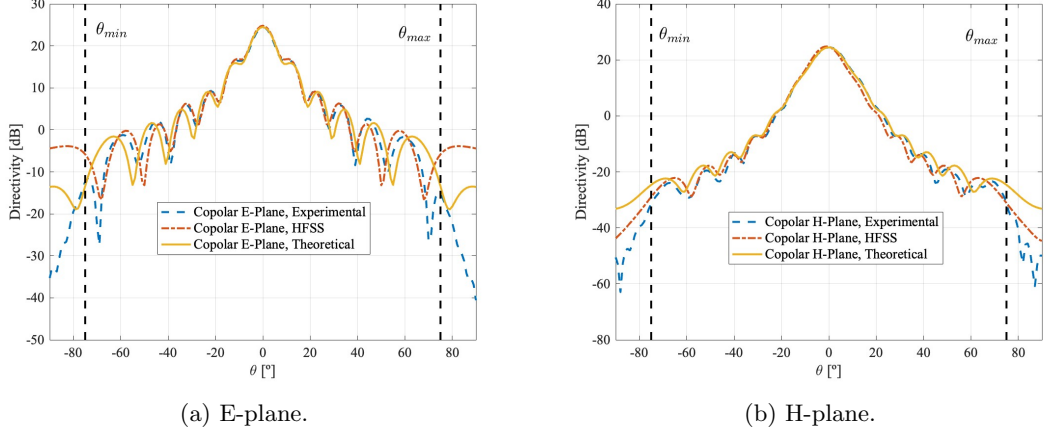


Figure 16: Ka-band radiation pattern comparison between the theoretical, simulated and experimental results.

The most important conclusion that can be drawn from the analysis of these data is how close and similar the simulated radiation pattern is with the experimental one. It can be seen how the yellow line (theoretical copolar component) for both planes is the one that, as theta increases, provides a more distant pattern to the rest. This is mainly due to the initial theoretical conditions explained in Section 2.1, where the theoretical analysis was carried out assuming an aperture arranged on an infinite ground from which the equivalent currents were obtained. On the other hand, the experimental and simulated results are closer to each other, especially in the  $[-40, 40]^{\circ}$  range, because they both do take into account the whole structure of the antenna so diffractions/fringing and different sources of the cross-polarization of a real horn are analyzed.

#### 2.4.2 C-band comparison

After performing the same type of comparison for the C-band AUT, conclusions can be drawn that are quite similar to those discussed above. Therefore, once again, Figure 17 shows how the behaviour of the experimental and simulated patterns are the most similar, especially in the range comprising the first sidelobes for both E and H planes. More specifically, for this case, a maximum relative error equivalent to 1.81% has been found, which is higher than the one obtained in the previous antenna. All these deviations are mainly due to two reasons, the first one has already been discussed several times throughout the report, linked to the theoretical assumptions for the ideal calculation of the AUT; the second one refers to the slight differences between the simulated and experimental results, mainly because in the case simulated through HFSS the SGH is not restrained by any support and a truly idyllic free-space environment is simulated, which contrasts with the two setups observed in Figures 11 and 14. In addition, another small percentage of the error can also be explained by the small differences in frequencies analyzed in each of the three types of analysis, this event was already analyzed in Figure 12a where the radiation pattern was found to vary with higher and lower frequencies.

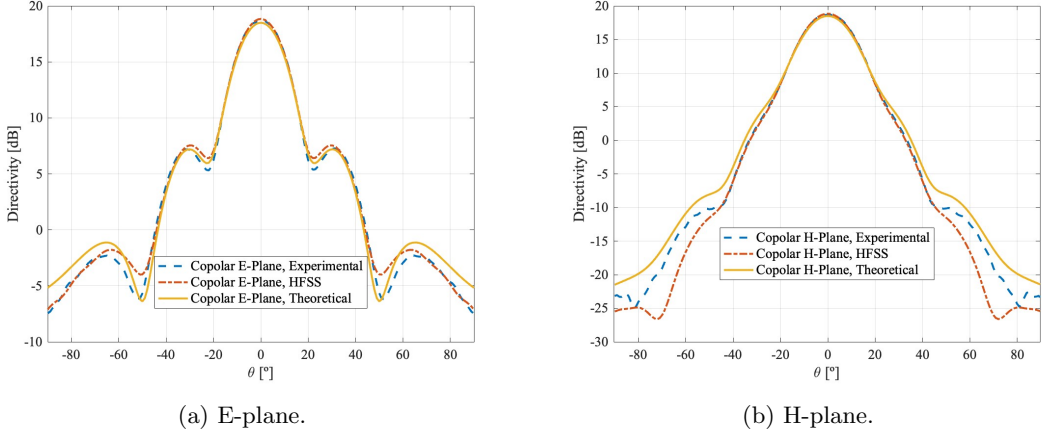


Figure 17: C-band radiation pattern comparison between the theoretical, simulated and experimental results.

### 3 Conclusion

The analysis of pyramidal horn antennas in the Ka and C frequency bands reveals consistent insights across approaches. Theory-based models provide a foundation for predicting antenna parameters, while simulations in HFSS allow deeper exploration into aspects such as diffraction and meshing effects. Experimental measurements confirm these findings, confirming the antennas' performance under real-world conditions. Pyramidal horn antennas are precision and adaptable for applications across varying frequency ranges, as demonstrated by these methodologies.

## Bibliography

- [1] Antenna measurements-part 2. Technical report.
  - [2] ANTENNA THEORY. Technical report.
  - [3] Samel Arslanagić 30430 Advanced Antenna Techniques and Measurements. Technical report, 2024.

## A Appendix

```

%% Balanis Equations for a Pyramidal Horn Antenna.
% Tomás Ruiz Aybar, AATM.

%% Ka-band Pyramidal Horn:

f = 32.5e9;
lambda = 3e8 / f;
a1 = 68.5e-3;
b1 = 56.5e-3;
D = sqrt(a1^2+b1^2);
p_e = 150e-3;
p_h = p_e;
b = 3.556e-3;
a = 7.112e-3;

% Angular variables
dthe = 1; dphi = 2; % angular increments
phi = (0:dphi:360)*(pi/180); % from 0 to 360
theta = (0:dthe:90)*(pi/180); % from 0 to 90
[THE, PHI] = meshgrid(theta, phi);

% Axial lengths, use 13-47a/b
rho_e = b1*sqrt((p_e/(b1-b))^2 + 1/4);
rho_h = a1*sqrt((p_h/(a1-a))^2 + 1/4);

%phi_e = rad2deg(asin((b1/2)/rho_e));
%phi_h = rad2deg(asin((a1/2)/rho_h));
rho_1 = sqrt(rho_e^2 - (b1^2/4));
rho_2 = sqrt(rho_h^2 - (a1^2/4));

E0 = 1;
r = 2*(2*D^2)/lambda; % Verify FF conditions
k = (2*pi)/lambda;

% This section has a high cost-computational cost

% eq.[13-25, 13-26]
k_primeX = k*sin(THE).*cos(PHI) + (pi/a1);
t2_prime = sqrt(1/(pi*k*rho_2))*((k*a1)/2 - k_primeX*rho_2);
t1_prime = sqrt(1/(pi*k*rho_2))*(-(k*a1)/2 - k_primeX*rho_2);
Ct2_prime = fresnelc(t2_prime);
Ct1_prime = fresnelc(t1_prime);
St2_prime = fresnels(t2_prime);
St1_prime = fresnels(t1_prime);

k_2primeX = k*sin(THE).*cos(PHI) - (pi/a1);
t2_2prime = sqrt(1/(pi*k*rho_2))*((k*a1)/2 - k_2primeX*rho_2);
t1_2prime = sqrt(1/(pi*k*rho_2))*(-(k*a1)/2 - k_2primeX*rho_2);
Ct2_2prime = fresnelc(t2_2prime);
Ct1_2prime = fresnelc(t1_2prime);
St2_2prime = fresnels(t2_2prime);

```

```

St1_2prime = fresnels(t1_2prime);

% eq.[13-5, 13-8]
k_Y = k*sin(THE).*sin(PHI);
t1 = sqrt(1/(pi*k*rho_1))*(-(k*b1)/2 - k_Y*rho_1);
t2 = sqrt(1/(pi*k*rho_1))*((k*b1)/2 - k_Y*rho_1);
Ct2 = fresnelc(t2);
Ct1 = fresnelc(t1);
St2 = fresnels(t2);
St1 = fresnels(t1);

% eq.[13-44]
I1 = 0.5*sqrt((pi*rho_2)/k).*exp(j.*((k_primeX.^2*rho_2)/(2*k)). ...
    *((Ct2_prime-Ct1_prime)-j.*((St2_prime-St1_prime))) + ... 
    exp(j.*((k_2primeX.^2*rho_2)/(2*k)).*((Ct2_2prime-Ct1_2prime)-j. ...
    *(St2_2prime-St1_2prime)));

% eq.[13-45]
I2 = sqrt((pi*rho_1)/k).*exp(j.*((k_Y.^2*rho_1)/(2*k)). ...
    *((Ct2-Ct1)-j.*((St2-St1))));

% E field components
Ethe = j*(k*E0*exp(-j*k*r))/(4*pi*r).*sin(PHI).*((1+cos(THE)).*I1.*I2);
Ethe = Ethe./max(max(abs(Ethe)));

Ephi = j*(k*E0*exp(-j*k*r))/(4*pi*r).*cos(PHI).*((cos(THE)+1).*I1.*I2);
Ephi = Ephi./max(max(abs(Ephi)));

% Plotting of far-field patterns

% Ludwig Co-Cx components
phi0 = 90*(pi/180);
Eco = Ethe.*cos(PHI-phi0) - Ephi.*sin(PHI-phi0);
Ecx = Ethe.*sin(PHI-phi0) + Ephi.*cos(PHI-phi0);

% Angular plotting variables
vthe = -90:dthe:90;
%vthe = [-fliplr(THE(1,2:end)), THE(1,:)];
vphi = 0:dphi:360-dphi;

% Find phi-indeces of E/H main planes
phi000 = 1;
phi090 = find(abs(vphi-90)<1e-3);
phi180 = find(abs(vphi-180)<1e-3);
phi270 = find(abs(vphi-270)<1e-3);
%phi090 = find(abs(PHI(:,1)-90)<1e-3);
%phi180 = find(abs(PHI(:,1)-180)<1e-3);
%phi270 = find(abs(PHI(:,1)-270)<1e-3);

% Co-polar and cx-polar phi=0 (H-plane)
Eco00 = [fliplr(Eco(phi180, 2:end)) Eco(phi000, :)];
Ecx00_t = [fliplr(Ecx(phi180, 2:end)) Ecx(phi000, :)];

```

```
% Co-polar and cx-polar phi=90 (E-plane)
Eco90 = [fliplr(Eco(phi270, 2:end)) Eco(phi090, :)];
Ecx90_t = [fliplr(Ecx(phi270, 2:end)) Ecx(phi090, :)];

% Directivity
%D = Directivity(Ethe, Eph, vthe, vphi);
%D0 = 10*log10(max(max(D)));
u = (1/sqrt(2))*((sqrt(lambda*rho_2))/a1 + (a1/sqrt(lambda*rho_2)));
v = (1/sqrt(2))*((sqrt(lambda*rho_2))/a1 - (a1/sqrt(lambda*rho_2)));
Cu = fresnelc(u);
Cv = fresnelc(v);
Su = fresnels(u);
Sv = fresnels(v);
aux = b1/(sqrt(2*lambda*rho_1));
C2 = fresnelc(aux)^2;
S2 = fresnels(aux)^2;
Dp = (8*pi*rho_1*rho_2)/(a1*b1)*((Cu-Cv)^2 + (Su - Sv)^2)*(C2 + S2);
D0 = 10*log10(max(max(Dp)));

figure();
hold on;
plot(vthe, D0+20*log10(abs(Eco00)), LineWidth=2)
plot(vthe, D0+20*log10(abs(Eco90)), LineWidth=2)
%plot(vthe, D0+20*log10(abs(Ecx00_t)), LineWidth=2)
%plot(vthe, D0+20*log10(abs(Ecx90_t)), LineWidth=2)
%plot(vthe_javier, 10*log10(abs(Eco00_javier)), 'b:', LineWidth=2)
%plot(vthe_javier, 10*log10(abs(Eco90_javier)), 'r:', LineWidth=2)
grid on;
xlim([-90 90])
ylabel('Directivity [dB]', 'FontName', 'Times New Roman', 'FontSize', 14)
xlabel('\theta [ ]', 'FontName', 'Times New Roman', 'FontSize', 14)
%legend('Copolar H-Plane, \phi = 0 ', 'Copolar E-Plane, \phi = 90 ', ...
%       'Copolar H-Plane, \phi = 0 ', 'Copolar E-Plane, \phi = ...
%       90 ', 'Javier H-Plane', 'Javier E-Plane', ...
%       'FontName', 'Times New Roman', 'FontSize', 14)
legend('Copolar H-Plane, \phi = 0 ', 'Copolar E-Plane, \phi = 90 ', ...
       'FontName', 'Times New Roman', 'FontSize', 14)
set(gca, 'FontName', 'Times New Roman', 'FontSize', 14)
```

Code 1: Matlab code to compute the theoretical approach for the radiated fields based on Balanis equations

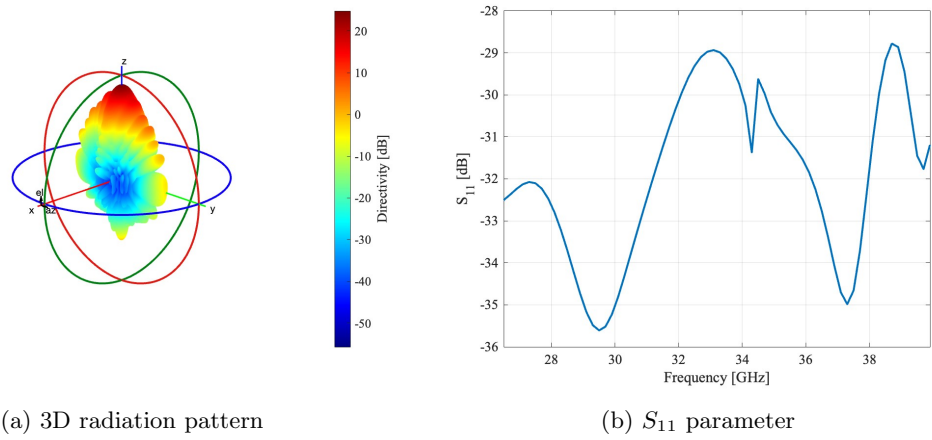


Figure 18: Different Ka-band parameters obtained through HFSS.

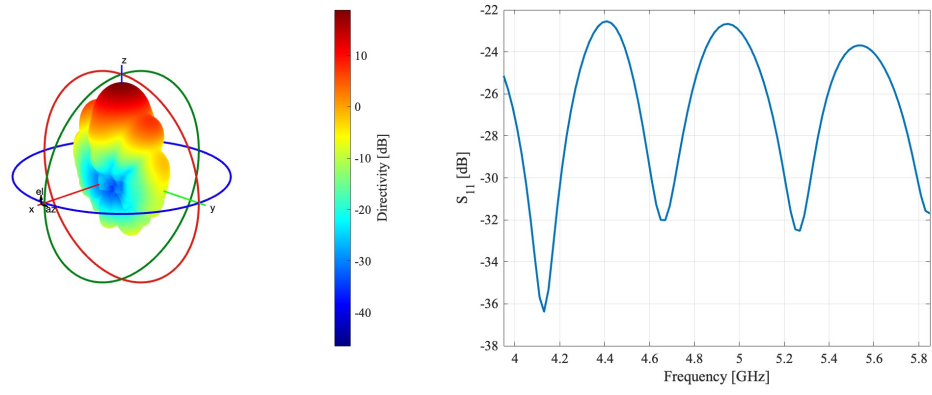


Figure 19: Different C-band parameters obtained through HFSS.